

# Dynamics-aware Adversarial Attack of Adaptive Neural Networks

An Tao  , Graduate Student Member, IEEE, Yueqi Duan  , Member, IEEE, Yingqi Wang  , Jiwen Lu  , Senior Member, IEEE, and Jie Zhou  , Senior Member, IEEE

**Abstract**—In this paper, we investigate the dynamics-aware adversarial attack problem of adaptive neural networks. Most existing adversarial attack algorithms are designed under a basic assumption – the network architecture is fixed throughout the attack process. However, this assumption does not hold for many recently proposed adaptive neural networks, which adaptively deactivate unnecessary execution units based on inputs to improve computational efficiency. It results in a serious issue of lagged gradient, making the learned attack at the current step ineffective due to the architecture change afterward. To address this issue, we propose a Leaded Gradient Method (LGM) and show the significant effects of the lagged gradient. More specifically, we reformulate the gradients to be aware of the potential dynamic changes of network architectures, so that the learned attack better “leads” the next step than the dynamics-unaware methods when network architecture changes dynamically. Extensive experiments on representative types of adaptive neural networks for both 2D images and 3D point clouds show that our LGM achieves impressive adversarial attack performance compared with the dynamic-unaware attack methods.

**Index Terms**—Adversarial attack, adaptive neural network, leaded gradient method

## I. INTRODUCTION

OVER the past decade, deep neural networks (DNNs) have significantly improved the performance of many computer vision tasks. In the context of this tremendous success, researchers are surprised to discover that DNNs are vulnerable to adversarial attacks [1], [2], which conceals a great security risk in real-world applications of DNNs. With small but carefully designed perturbations on input examples, attackers can easily force a well-trained model to make mistakes. Various methods are proposed to better attack DNNs and analyze their weaknesses [2]–[4].

Most existing adversarial attack methods assume that the network architecture is fixed throughout the attack process, which ensures a static data inference path to guarantee the effectiveness of the attack at every step. However, this assumption does not hold if the network can adapt its architecture to

An Tao, Jiwen Lu, and Jie Zhou are with the Department of Automation, Tsinghua University, Beijing 100084, China, and also with the Beijing National Research Center for Information Science and Technology (BNRist), Beijing 100084, China (e-mail: ta19@mails.tsinghua.edu.cn; lujiwen@tsinghua.edu.cn; jzhou@tsinghua.edu.cn).

Yueqi Duan is with the Department of Electronic Engineering, Tsinghua University, Beijing 100084, China (e-mail: duanyueqi@tsinghua.edu.cn).

Yingqi Wang is with the Xinya College, Tsinghua University, Beijing 100084, China (e-mail: yingqi-w19@mails.tsinghua.edu.cn).

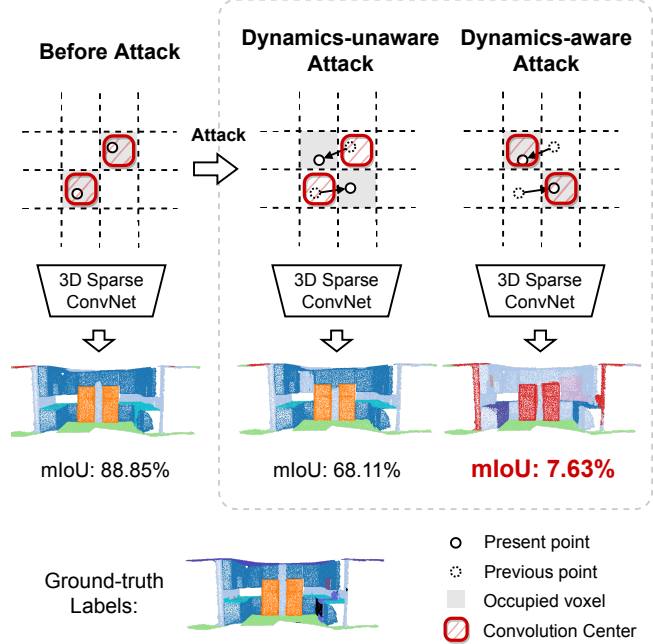


Fig. 1. An illustration of the benefit of dynamics-aware attack on 3D sparse convolution network for point clouds. If a voxel does not contain point(s) and disappears after one attack step, the convolution on this voxel will become invalid. This change in network architecture causes the learned perturbation by the dynamics-unaware attack may not be efficient to the changed new architecture. Instead, our dynamics-aware attack considers the dynamic change of the positions of convolution kernels after attack and achieves remarkably lower mIoU on the presented point cloud scene.

different inputs, i.e., Adaptive Neural Network. Adaptive neural networks own advantages in terms of accuracy and computational efficiency by adaptively deactivating unnecessary input-dependent execution units. When we learn adversarial perturbations at each step, the network architecture changes after we add the perturbations to the input, so the attack may not be effective due to the change of the target network. We summarize this issue as **lagged gradient** – we cannot foresee the changed network architecture to back-propagate the effective attack gradients at the current step.

In this paper, we employ two typical types of adaptive neural networks to study the lagged gradient issue in the adversarial attack of adaptive neural networks, including layer skipping network [5] and 2D/3D sparse convolution network [6], [7]. Visual data usually distribute sparsely in some views, such as easy/hard to recognize in sample-wise

or informative/uninformative areas in spatial-wise. Instead of using a fixed intact network to tackle all data, layer skipping network and sparse convolution network are two representative network types that can adapt their network architecture to the two above kinds of sparse distribution. Layer skipping network can bypass unnecessary network layers according to inputs. For challenging hard images, the network executes more layers than easy images. In contrast to layer skipping network that allocates computation resources layer-wise, sparse convolution network allocates convolutions spatially within the layer. 2D sparse convolution network predicts a spatial pixel-wise binary mask and deactivates the convolutions that operate on invalid pixels. For 3D point clouds, after converting 3D point clouds into a number of occupied voxels in the 3D grid, 3D sparse convolution network deactivates convolutions that center on unnecessary voxels, i.e. unoccupied voxels. In Fig. 1, we take 3D sparse convolution network as a typical example to illustrate the lagged gradient issue of adaptive neural networks. Because the convolution operation of 3D sparse convolution network depends on the locations of occupied voxels, the attack learned at time  $t$  may not be effective due to the dynamic changes of network architecture at time  $t + 1$ .

To address this issue, we propose a Leaded Gradient Method (LGM) for dynamics-aware adversarial attack of adaptive neural networks. We first model the input-dependent execution units into a general form of normal execution units, where we bring in input-dependent occupancy values as the mask to represent whether each unit is valid or not. In this way, although the computation results of the deactivated execution units still keep zero due to the zero occupancy values, they are enabled to propagate non-zero gradients through the occupancy values. Then, we reformulate the received gradient through the network that also includes the changes of the input-dependent execution units caused by input perturbations in adversarial attack, so that the learned attack is dynamics-aware as the input-dependent occupancy values can be considered as hyper-parameters of the adaptive neural network. Finally, we carefully design differentiable algorithms to approximate the non-differentiable occupancy values, where we can learn the attack in an end-to-end differentiable manner. Additionally, since our LGM reformulates the received gradient itself to tailor the dynamic property of adaptive neural networks, it can be easily combined with existing adversarial attack methods to achieve better attack performance on adaptive neural networks.

We conduct extensive adversarial attack experiments on representative types of adaptive neural networks with various 2D image datasets (CIFAR-10 [8] and ImageNet [9]) and 3D point cloud datasets (ScanNet [10], S3DIS [11], [12], and SemanticKITTI [13]). In all the experiments, our dynamics-aware attack achieves impressive attack performance, and also significantly outperforms the baseline dynamics-unaware method. We also analyze the influence of attacks on network architecture and give qualitative visualizations of attack results.

Our key contributions are summarized as follows:

- 1) To our best knowledge, we are the first to discover the lagged gradient issue in the adversarial attack of adaptive neural networks. Because the network can adapt

its architecture to different inputs, the normally learned attack at time  $t$  may not be effective due to the dynamic changes of network architecture at time  $t + 1$ .

- 2) We design a Leaded Gradient Method (LGM) for the dynamics-aware adversarial attack of adaptive neural networks by reformulating the received gradients to be aware of the potential dynamic changes of network architectures. Therefore, the learned gradients can better “lead” the next attack step than the dynamics-unaware attacks.
- 3) Experimental results on various adaptive neural networks and datasets show that our dynamics-aware attack achieves impressive attack performance compared with the baseline dynamics-unaware methods.

## II. RELATED WORK

In this section, we briefly review two related topics: 1) adversarial attack, and 2) adaptive neural network.

### A. Adversarial Attack

Adversarial examples for deep neural networks are first discovered by Szegedy *et al.* [1]. Goodfellow *et al.* [2] then proposed a Fast Gradient Sign Method (FGSM) to directly generate adversarial examples by adding the clean example with an imperceptibly small vector whose elements are equal to the sign of the back-propagated gradient. Iterative FGSM (I-FGSM) [14], Projected Gradient Descent (PGD) [15], and Carlini-Wagner attack (C&W) [4] are three representative extensions that utilize gradient descent to optimize the objective function. Other effective attacks include box-constrained L-BFGS [1], Jacobian-based Saliency Map Attack (JSMA) [16], and DeepFool [3]. The above methods are white-box attacks, where the attacker knows the architecture and weight of the victim models. Considering the details of the models are not usually accessible to attackers, some works focus on black-box attacks in which the attacker has no knowledge of the model architecture or weight [17]–[20].

After the adversarial attack is explored in 2D images, some works also focus on 3D point cloud attacks. Xiang *et al.* [21] first propose two types of adversarial attacks on point clouds: adversarial point perturbation and adversarial point generation. Recently, many 3D attacks are proposed [22]–[26] and achieve impressive attack performance.

Some recent works study adversarial attacks on adaptive neural networks, but their attack goal is to slow down the network inference speed. By adjusting the objective function to be related to the network’s energy consumption, adaptive neural networks can be fooled to activate more execution units [27]–[29]. These methods all ignore the network architecture change when performing attack. To our best knowledge, we are the first to discover the lagged gradient issue of adaptive neural networks and show its great impact.

### B. Adaptive Neural Network

As many successful deep neural networks are proposed and playing an important role in various areas [30]–[34], researchers begin to focus on how to design the network more

efficient and propose adaptive neural networks [35]. Different from the traditional static neural networks that conduct same computations for all inputs, adaptive neural networks can change their network architecture by selectively activating a portion of computation units that fit the demand of the input. Since not all computation units are required during network inferences, adaptive neural networks can be more efficient than static neural networks.

Adaptive neural networks change their architectures mainly in two ways, i.e. depth and width. For depth changing, early exiting [36] and layer skipping [5], [37] are two representative methods, allowing easy input examples to execute fewer number of network layers but also achieving state-of-the-art accuracy. The network's width can be changed within the layer in terms of neurons [38], channels [39], and branches [40].

Considering the informative areas of visual data usually do not cover all spaces and distribute sparsely, adaptive neural networks can also allocate their computation resources in a spatial view, including sparse convolution [6], [41], additional refinement [42], region localization [43], and resolution scaling [44]. Among the various network designs, it's worth noting that 3D sparse convolution network [7] is a representative, popular and powerful network type in 3D point cloud processing and achieves impressive performance in large-scale point cloud scenes. Recently, 3D sparse convolution network is becoming a dominant network type in 3D semantic segmentation [45]–[47], instance segmentation [48], [49] and object detection [50]–[52] on various indoor and outdoor large-scale point cloud scene datasets for self-driving cars and indoor robots and achieve state-of-the-art performance.

### III. DYNAMICS-AWARE ADVERSARIAL ATTACK

In this section, we first illustrate the nature of the lagged gradient issue in adaptive neural networks. Then, we propose a dynamics-aware adversarial attack to tackle the issue by using a Leaded Gradient Method (LGM). Note that in this section we only give the general formulation of LGM in our attack. We give attack applications on representative adaptive neural networks in the next section.

#### A. Lagged Gradient Issue

White-box attack is a basic attack form that utilizes the gradients throughout the victim network. Based on the received gradients, attackers can design various optimization algorithms [3], [14] and objective functions [4] to achieve better performance. The quality of gradients is crucial in attacks, but gradients are not useful in all cases. The gradient can disappear due to non-differentiable functions, e.g., flooring and binarization, can be stochastic in randomized neural networks, and can be exploding/vanishing in extremely deep neural network [53].

In this work, we consider a normal neural network that can back-propagate the non-zero non-randomized steady gradient. Although the gradient seems useful in the attack, we show that the gradient may still be ineffective in the attack. We first study the mapping between the input and the output of classical vision neural networks, e.g., AlexNet [30], VGG [31],

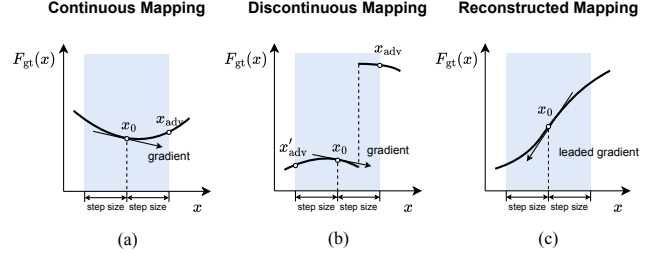


Fig. 2. An illustration of the ineffective attack in both the (a) continuous and (b) discontinuous mapping between the network's input  $x$  and output logit  $F_{gt}(x)$  on the ground-truth class. In this paper, we summarize the gradient issue in (b) as the lagged gradient caused by the network architecture change in adaptive neural networks. We propose a dynamics-aware attack that reconstructs the mapping to reformulate the back-propagated gradient as the leaded gradient in (c) to be aware of the potential network architecture change. With the guide of the leaded gradient in (c), we obtain  $x'_{adv}$  in (b) which satisfies  $F_{gt}(x'_{adv}) < F_{gt}(x_0)$ . In this figure, we consider the input  $x$  as a one-dimensional variable for simplicity and try to decrease the output logit  $F_{gt}(x)$  through the attack.

and ResNet [33]. The mapping is continuous in nature, since the forward propagation in the neural network is basically composed of the four fundamental operations of arithmetic. Although some functions like ReLU [54] and max-pooling are piecewise, their outputs are still continuous at the demarcation points. In Fig. 2 (a), we show that the gradient may mislead the attack in the continuous mapping between the network's input  $x$  and output logit  $F_{gt}(x)$  on the ground-truth class. The attacker follows the gradient direction at the current point  $x_0$  to obtain a nearby point  $x_{adv}$  and assumes that  $x_{adv}$  can achieve a lower network output. The assumption may not be correct at any time, since the gradient of the current point  $x_0$  cannot determine the status of the network output at the nearby point  $x_{adv}$ . The issue can be weakened easily through a smaller step size, since the mapping is usually smooth local. If the mapping dramatically fluctuates in local, using second-order derivatives during optimization can help. This ineffective gradient issue is not serious enough and does not cause a significant effect on attack performance.

However, the ineffective gradient issue can be non-negligible in the discontinuous mapping caused by the network architecture change in adaptive neural networks. In Fig. 2 (b), if the attacker follows the normally learned gradient direction at the current point  $x_0$  and moves to  $x_{adv}$ , it can be difficult to turn back to the left part of the mapping in the subsequent iterations. Due to the noteworthy network architecture change, the gradient at the current point  $x_0$  is not only ineffective but also lags behind the architecture change. We summarize the gradient issue specific in adaptive neural networks as **lagged gradient**. The strategies to weaken the gradient issue in continuous mapping can fail in discontinuous mapping, since they are usually built on local derivatives and cannot specifically foresee the discontinuous network architecture change. In contrast, we propose a dynamics-aware adversarial attack by reconstructing the mapping to reformulate the gradient as **leaded gradient** in Fig. 2 (c) that is able to be aware of the network architecture change. With the guide of the leaded gradient, we obtain a new adversarial point  $x'_{adv}$  that satisfies  $F_{gt}(x'_{adv}) < F_{gt}(x_0)$ . In the following content, we give a

general form of our dynamics-aware adversarial attack on how to formulate the leaded gradient during the attack.

### B. Attack against Input-adaptive Computation Unit

**Input-adaptive Computation Unit.** Since adaptive neural networks can selectively activate a portion of computation units (e.g. neurons [38], convolutions [7], [55], layers [5], [37], and network blocks [40], [56]) based on different inputs, we consider one specific input-dependent computation unit within the network and denote it in a general form  $\Phi(\cdot)$ . We define the input of the whole network as  $\mathbf{x}$  and an intermediate feature within the network as  $\mathbf{f}$ . The unit's operating formula can be written as:

$$\mathbf{f}' = \Phi(\mathbf{f}) \quad \text{for } \mathbf{x} \in \mathcal{A}, \quad (1)$$

where  $\mathbf{x} \in \mathcal{A}$  denotes the input  $\mathbf{x}$  satisfies some conditions and therefore  $\mathbf{x}$  belongs to an assemble  $\mathcal{A}$ . If the input-dependent unit is valid, it transforms the feature  $\mathbf{f}$  by  $\Phi(\mathbf{f})$ , else the output  $\mathbf{f}$  is vacant to save memory. Note that in some cases, such as 2D sparse convolution, the output feature  $\mathbf{f}'$  exists and is set as zero when the computation unit  $\Phi(\cdot)$  is not executed.

**Fast Gradient Method (FGM).** We first illustrate the traditional gradient propagation manner in existing adversarial attacks and name it as Fast Gradient Method (FGM). Existing adversarial attacks assume that the victim network has a fixed network architecture. When these attacks are performed on adaptive neural networks, they in essence treat the judgment result in (1) fixed to propagate gradients. To better illustrate this effect, we alleviate the judgement condition  $\mathbf{x} \in \mathcal{A}$  into an occupancy function  $o(\mathbf{x}) \in \{0, 1\}$  and use it as the mask of the computation unit  $\Phi(\cdot)$ . Because the output of  $o(\mathbf{x})$  is binary and cannot propagate valid gradient into  $\mathbf{x}$ , the traditional gradient propagation manner ignores the potential changes of the  $o(\mathbf{x})$  during attack and takes its output as a constant value  $\bar{o}$ . In this case, (1) becomes:

$$\mathbf{f}'_{\text{FGM}} = \bar{o} \cdot \Phi(\mathbf{f}), \quad (2)$$

where  $\mathbf{f}'_{\text{FGM}}$  equals to  $\mathbf{f}'$  in (1). The partial derivative of  $\mathbf{f}'_{\text{FGM}}$  with respect to  $\mathbf{x}$  is:

$$\frac{\partial \mathbf{f}'_{\text{FGM}}}{\partial \mathbf{x}} = \bar{o} \cdot \frac{\partial \Phi(\mathbf{f})}{\partial \mathbf{x}}. \quad (3)$$

**Leaded Gradient Method (LGM).** FGM has an apparent shortage in adaptive neural networks. Since the occupancy  $\bar{o}$  may be changed after an attack step, the gradient in (3) does not consider the dynamic changes in network architecture. The learned attack based on the gradient of the current time may not be effective on the new architecture after this attack step. To be aware of this dynamic change, we propose Leaded Gradient Method (LGM) to reformulate the gradient. Specifically, we replace  $\bar{o}$  with the function  $o(\mathbf{x})$ . Therefore, (2) becomes:

$$\mathbf{f}'_{\text{LGM}} = o(\mathbf{x}) \cdot \Phi(\mathbf{f}). \quad (4)$$

The occupancy function  $o(\mathbf{x})$  is able to propagate gradient with respect to input  $\mathbf{x}$ . The partial derivative of  $\mathbf{f}'_{\text{LGM}}$  becomes:

$$\frac{\partial \mathbf{f}'_{\text{LGM}}}{\partial \mathbf{x}} = \bar{o} \cdot \frac{\partial \Phi(\mathbf{f})}{\partial \mathbf{x}} + \frac{\partial o(\mathbf{x})}{\partial \mathbf{x}} \cdot \Phi(\mathbf{f}). \quad (5)$$

Compared with the traditional gradient calculation in (3) that does not consider dynamic architecture changes, we can discover that (5) has one more derivative on  $\frac{\partial o(\mathbf{x})}{\partial \mathbf{x}}$ , which ensures the existence change of computation unit  $\Phi(\cdot)$  is reflected in the back-propagated gradients.

**Non-differentiable Function Approximation.** Since the hard occupancy  $o(\mathbf{x})$  is binary in value, its gradient quality would be poor. To solve this issue, we follow the Backward Pass Differentiable Approximation (BPDA) method in [53] to present a differentiable function  $\hat{o}(\mathbf{x})$  to replace  $o(\mathbf{x})$  in gradient back-propagation. For the network's forward propagation, we can either adopt  $o(\mathbf{x})$  or  $\hat{o}(\mathbf{x})$ . In this work, we choose to replace  $o(\mathbf{x})$  with  $\hat{o}(\mathbf{x})$  in forward propagation due to its superior performance. When designing  $\hat{o}(\mathbf{x})$ , we present three important criteria:

- 1) The output value of the differentiable function  $\hat{o}(\mathbf{x})$  should be similar to the original hard function  $o(\mathbf{x})$  in most areas, so  $\hat{o}(\mathbf{x})$  can substitute  $o(\mathbf{x})$  in both forward and backward propagation;
- 2) The differentiable function  $\hat{o}(\mathbf{x})$  should have significant gradient variation near the decision boundary of  $o(\mathbf{x})$ ;
- 3) The gradient of the differentiable function  $\hat{o}(\mathbf{x})$  should be smooth and lie in a reasonable range to avoid the gradient vanishing or exploding.

Because of the diversity of adaptive neural networks, the modeling manner of occupancy function  $o(\mathbf{x})$  in (4) and the differentiable soft occupancy function  $\hat{o}(\mathbf{x})$  can be varied. In the following contents, we show the application of dynamics-aware adversarial attacks in specific networks.

## IV. ATTACK AGAINST ADAPTIVE NEURAL NETWORKS

In this section, we take layer skipping network and 2D/3D sparse convolution network as examples to show the application of dynamics-aware adversarial attack in specific adaptive neural networks. We first present the attack in layer skipping network [5]. Next, we show the attack in 2D sparse convolution network [6]. Finally, we extend the application of attack into 3D sparse convolution network [7]. Note that the variable names in different sections and subsections can be varied.

### A. Attack against Layer Skipping Network

Layer skipping network [5], [37] is a representative type of adaptive neural network that changes the network architecture in depth. The network can skip more layers when processing easy input examples but still achieves state-of-the-art accuracy. To make the skipping decisions of skippable network layers, the network needs to learn a series of binary occupancy values. Given an input image  $\mathbf{X}$ , the network forward propagation can be described as follows:

$$\mathbf{y} = (o^L \circ H^L) \circ (o^{L-1} \circ H^{L-1}) \circ \dots \circ (o^1 \circ H^1)(\mathbf{X}), \quad (6)$$

where the network consists of  $L$  skippable layers, and  $o^l \in \{0, 1\}$  is an occupancy value determining the execution of layer  $H^l$ ,  $1 \leq l \leq L$ . Note that in (6) we only show the skippable layers, the network may also contain static layers.

In order to detail our dynamics-aware attack, we focus on an arbitrary layer skippable  $H(\cdot)$ . We first describe the process to

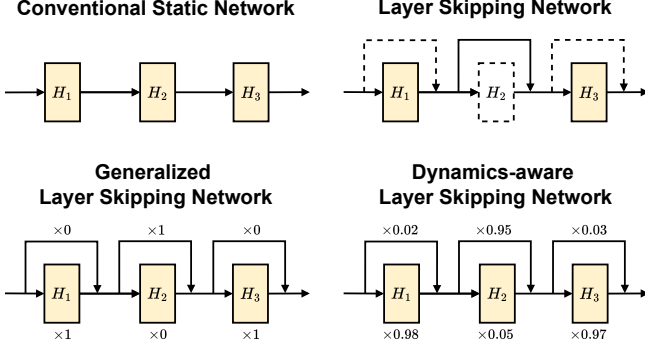


Fig. 3. An illustration of the conventional static network that feeds the data through all layers, layer skipping network in (6) that adopts the module in (9), generalized layer skipping network that adopts the module in (11), and our dynamics-aware layer skipping network that adopts the module in (13) with soft occupancy. In the figure, we show the network that only contains three skippable layers for simplicity.

obtain the decision of this layer. Then we detail our dynamics-aware attack on layer  $H(\cdot)$ .

**Preliminary.** Given an input image  $\mathbf{X} \in \mathbb{R}^{H_0 \times W_0 \times 3}$  and a intermediate feature map  $\mathbf{F} \in \mathbb{R}^{H \times W \times D}$ , we learn a binary occupancy  $o \in \{0, 1\}$  that controls the decision to whether execute the following skippable layer, which is obtained as the indicator function  $\mathbf{1}$  in (6). Similar to 2D sparse convolution, the process to learn the occupancy can be broken into two steps: 1) use an occupancy generation network  $G(\cdot)$  to output an occupancy score  $q \in \mathbb{R}$ ; 2) binary the score  $q$  into hard occupancy  $o$  by only retaining the sign. The formulations are as follows:

$$q = G(\mathbf{F}), \quad (7)$$

$$o = \text{sign}(q). \quad (8)$$

We can summarize (7-8) into an occupancy function  $o(\mathbf{F})$ . Note that in some designs the occupancy generation network  $G(\cdot)$  may input several feature maps from different previous layers. In this paper, we only consider the simplest formulation that only requires the latest feature map  $\mathbf{F}$  for clarity.

**Layer Skipping Module.** With the binary occupancy  $o$ , we can decide whether to skip the following layer  $H(\cdot)$ . If  $o = 1$ , layer  $H(\cdot)$  still operates and outputs a new feature map  $\mathbf{F}'$ . Else, layer  $H(\cdot)$  is skipped and the output is vacant to save memory cost. The input of the next network layer  $H'(\cdot)$  is still  $\mathbf{F}$ . The formula of the layer skipping module is as follows:

$$\mathbf{F}' = H(\mathbf{F}) \text{ for } o = 1, \quad (9)$$

$$\mathbf{F}'' = \begin{cases} H'(\mathbf{F}'), & o = 1 \\ H'(\mathbf{F}), & o = 0 \end{cases}, \quad (10)$$

where  $\mathbf{F}''$  denotes the output feature map of the network layer  $H'(\cdot)$  that directly follows the current network layer  $H(\cdot)$ . For simplicity, we consider  $H'(\cdot)$  as a non-skippable network layer in (10).

**FGM in Layer Skipping Module.** To detail our attack, we reformulate the formulas in (9-10) into a general form. In FGM, we take the occupancy  $o$  as a constant value  $\bar{o}$ , and rewrite the formulas as:

$$\mathbf{F}' = \bar{o} \cdot H(\mathbf{F}) + (1 - \bar{o}) \cdot \mathbf{F}. \quad (11)$$

Therefore, the feature map  $\mathbf{F}'$  exists in all cases, and the input of the next network layer  $H'(\cdot)$  can be fixed with  $\mathbf{F}'$ . The partial derivative of  $\mathbf{F}'$  with respect to the input image  $\mathbf{X}$  is:

$$\frac{\partial \mathbf{F}'}{\partial \mathbf{X}} = \bar{o} \cdot \frac{\partial H(\mathbf{F})}{\partial \mathbf{X}} + (1 - \bar{o}) \cdot \frac{\partial \mathbf{F}}{\partial \mathbf{X}}. \quad (12)$$

**LGM in Layer Skipping Module.** To allow the gradient to be aware of the changes of occupancies, we let the occupancy  $o$  also propagate the gradient into the input image  $\mathbf{X}$  through  $o(\mathbf{F})$ . We rewrite the formula in (11) as follows:

$$\mathbf{F}' = o(\mathbf{F}) \cdot H(\mathbf{F}) + (1 - o(\mathbf{F})) \cdot \mathbf{F}. \quad (13)$$

The partial derivative of  $\mathbf{F}'$  with respect to the input image  $\mathbf{X}$  is:

$$\frac{\partial \mathbf{F}'}{\partial \mathbf{X}} = \bar{o} \cdot \frac{\partial H(\mathbf{F})}{\partial \mathbf{X}} + (1 - \bar{o}) \cdot \frac{\partial \mathbf{F}}{\partial \mathbf{X}} + \frac{\partial o(\mathbf{F})}{\partial \mathbf{X}} \cdot H(\mathbf{F}) - \frac{\partial o(\mathbf{F})}{\partial \mathbf{X}} \cdot \mathbf{F}. \quad (14)$$

Compared to traditional fast gradient calculation in (12), the partial derivative in (14) has two more terms on  $\frac{\partial o(\mathbf{F})}{\partial \mathbf{X}}$ , which reflects the dynamics changes when back-propagating gradients.

**Non-differentiable Function Approximation.** To calculate  $\frac{\partial o(\mathbf{F})}{\partial \mathbf{X}}$ , we release it into  $\frac{\partial o(\mathbf{F})}{\partial \mathbf{F}} \frac{\partial \mathbf{F}}{\partial \mathbf{X}}$ . Because  $o(\mathbf{F})$  is constructed by (7-8), we note that (8) is a non-differentiable function which leads poor gradient quality in  $\frac{\partial o(\mathbf{F})}{\partial \mathbf{F}}$ . Therefore, we release the sign function  $\text{sign}(\cdot)$  in (8) with a sigmoid function as:

$$\hat{o} = \frac{1}{1 + \exp(-\lambda \cdot q)}, \quad (15)$$

where  $\lambda$  is a parameter to control the slope. With the sigmoid function, we can rewrite the hard occupancy function  $o(\mathbf{F})$  as the released soft function  $\hat{o}(\mathbf{F})$  and use  $\hat{o}(\mathbf{F})$  in back-propagation.

## B. Attack against 2D Sparse Convolution Network

To discover the sparsely distributed informative areas, 2D sparse convolution network [6], [41] needs to learn a pixel-wise binary occupancy mask on the feature map to restrict the locations of the following sparse convolutions. We first introduce the process to obtain the pixel-wise binary occupancy mask and give the formula of 2D sparse convolution. Then, we detail our dynamics-aware attack on 2D sparse convolution.

**Preliminary.** Given an input image  $\mathbf{X} \in \mathbb{R}^{H_0 \times W_0 \times 3}$  and an intermediate feature map  $\mathbf{F} \in \mathbb{R}^{H \times W \times D}$ , we denote the learned binary occupancy mask on the feature map as  $\mathbf{O} \in \{0, 1\}^{H \times W}$ , which denotes the occupancies of convolution operation. The process to learn the occupancy matrix can be broken into two steps: 1) use an occupancy generation network  $G(\cdot)$  to output an occupancy score matrix  $\mathbf{Q} \in \mathbb{R}^{H \times W}$ ; 2) binary the score matrix  $\mathbf{Q}$  into hard occupancy  $\mathbf{O}$  by only retaining the elements' sign. The formulations are the same with (7-8). With the binary occupancy matrix  $\mathbf{O}$ , we can conduct convolutions that center on the locations of the valid elements in matrix  $\mathbf{O}$ .

**2D Sparse Convolution.** Consider a convolution kernel with weights  $\mathbf{W} \in \mathbb{R}^{C \times C \times D \times D'}$  and a bias  $\mathbf{b} \in \mathbb{R}^{D'}$ .

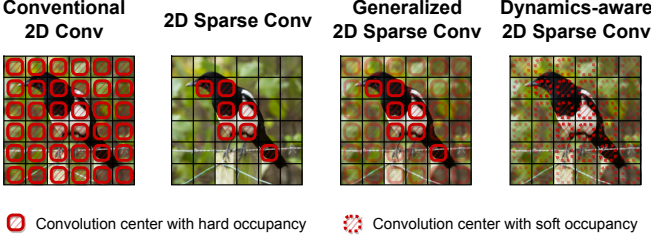


Fig. 4. An illustration of conventional 2D convolution that operates on every pixels, 2D sparse convolution in (16), generalized 2D sparse convolution in (17), and our dynamics-aware 3D sparse convolution in (19) with soft occupancy. We only draw the convolution center in this figure for concise, and the color shade indicates the magnitude of the convolution’s occupancy value. For simplicity, we draw the pixel-wise grid size as  $6 \times 6$ .

The weights  $\mathbf{W}$  can be broken down into spatial weights  $\mathbf{W}_u \in \mathbb{R}^{D \times D'}$  with  $C \times C$  matrices, where  $u \in \mathcal{S}$  is a coordinate offset. If  $C = 3$ , the kernel size is  $3 \times 3$  and  $\mathcal{S} = \{-1, 0, 1\}^2$ . To analyze pixel-wise operations, we broke down the occupancy  $\mathbf{O}$  into pixel-wise occupancy elements  $\{o_{[1,1]}, o_{[1,2]}, \dots, o_{[H,W]}\}$ , where each occupancy element belongs to  $\{0, 1\}$ . We also broke down the feature map  $\mathbf{F}$  into pixel-wise features  $\{f_{[1,1]}, f_{[1,2]}, \dots, f_{[H,W]}\}$ , where each feature vector belongs to  $\mathbb{R}^D$ . We consider a location vector  $\mathbf{p} = [h, w]$ , when it is valid in the occupancy, i.e.,  $m_p = 1$ , the convolution outputs feature  $f'_p \in \mathbb{R}^{D'}$  in location  $\mathbf{p}$ . Else, the network does not conduct convolution and therefore the output feature vector  $f'_p$  in the location  $\mathbf{p}$  is set as zero. The formula of 2D sparse convolution is as follows:

$$f'_p = \begin{cases} \sum_{u \in \mathcal{S}} W_u f_{p+u} + b, & o_p = 1 \\ 0, & o_p = 0 \end{cases}. \quad (16)$$

**FGM in 2D Sparse Convolution.** We release the 2D sparse convolution into a generalized convolution by multiplying a constant occupancy value  $\bar{o}_p$ . The value of  $\bar{o}_p$  is the same with  $o_p$ . In this case, the generalized 2D sparse convolution operates on every pixel in the feature map  $\mathbf{F}$  as:

$$f'_{\text{FGM}} = \bar{o}_p \cdot \left( \sum_{u \in \mathcal{S}} W_u f_{p+u} + b \right). \quad (17)$$

The partial derivative of  $f'_{\text{FGM}}$  with respect to the input image  $\mathbf{X}$  is:

$$\frac{\partial f'_{\text{FGM}}}{\partial \mathbf{X}} = \bar{o}_p \cdot \left( \sum_{u \in \mathcal{S}} W_u \frac{\partial f_{p+u}}{\partial \mathbf{X}} \right). \quad (18)$$

**LGM in 2D Sparse Convolution.** To be aware of the dynamic location of sparse convolution, we replace the constant value  $o_p$  with the occupancy element  $o_p$  which is derived by the function  $o_p(\mathbf{F})$ . Although  $o_p(\mathbf{F})$  and  $\bar{o}_p$  share the same values, the advantage of  $o_p(\mathbf{F})$  is that it can propagate gradient into input image  $\mathbf{X}$ . With the occupancy function  $o_p(\mathbf{F})$ , the formula of convolution is:

$$f'_{\text{LGM}} = o_p(\mathbf{F}) \cdot \left( \sum_{u \in \mathcal{S}} W_u f_{p+u} + b \right). \quad (19)$$

The partial derivative of  $f'_{\text{LGM}}$  with respect to the input image  $\mathbf{X}$  is:

$$\begin{aligned} \frac{\partial f'_{\text{LGM}}}{\partial \mathbf{X}} &= \bar{o}_p \cdot \left( \sum_{u \in \mathcal{S}} W_u \frac{\partial f_{p+u}}{\partial \mathbf{X}} \right) \\ &+ \frac{\partial o_p(\mathbf{F})}{\partial \mathbf{X}} \cdot \left( \sum_{u \in \mathcal{S}} W_u f_{p+u} + b \right). \end{aligned} \quad (20)$$

Compared to traditional fast gradient calculation in (18), the partial derivative in (20) has one more term on  $\frac{\partial o_p(\mathbf{F})}{\partial \mathbf{X}}$ , which ensures the propagated gradient is aware of the dynamic changes of convolutions.

**Non-differentiable Function Approximation.** Similar to the layer skipping network, we note that  $\frac{\partial o_p(\mathbf{F})}{\partial \mathbf{X}}$  can cause poor gradient quality because the non-differentiable  $\text{sign}(\cdot)$  function in (8). Following the practice in the layer skipping module, we release the  $\text{sign}$  function  $\text{sign}(\cdot)$  with a sigmoid function in (15) that outputs a soft occupancy value  $\hat{o}_p$ . We then replace the hard binary occupancy function  $o_p(\mathbf{F})$  with the released soft occupancy  $\hat{o}_p(\mathbf{F})$  in back-propagation.

### C. Attack against 3D Sparse Convolution Network

3D sparse convolution network [7] is a dominant network type in large-scale 3D point cloud analysis. To process point cloud data, 3D sparse convolution network transforms the point clouds into a number of occupied voxels in the 3D grid and only applies convolutions centered on these occupied voxels. Traditional point-based point cloud networks [57]–[63] directly process point clouds and are easy to explode in both computation and memory when querying neighbour points in a large-scale point cloud scene. In contrast, 3D sparse convolution network operates on the 3D grid to avoid the costs of neighbor searching and also keeps the sparsity throughout the network architecture by restricting the computation of convolutions to reduce resource costs. These two advantages lead to the popularity of 3D sparse convolution network in large-scale point cloud tasks. We first introduce 3D sparse convolution network by giving the formulation of 3D sparse convolution, and then detail our dynamics-aware attack on it.

**Preliminary.** Given a point cloud with  $N$  points, we define the set of point cloud XYZ coordinates  $\mathcal{X}^{\text{pt}} = \{\mathbf{x}_1^{\text{pt}}, \mathbf{x}_2^{\text{pt}}, \dots, \mathbf{x}_N^{\text{pt}}\} \in \mathbb{R}^{N \times 3}$ . After voxelization in 3D grid,  $N$  points are converted into  $M$  sparse voxels, where  $M \leq N$ . Each sparse voxel contains at least one point in the point cloud. Following the definitions above, we consider the set of normalized voxel XYZ coordinates  $\mathcal{X} = \{\mathbf{x}_1, \mathbf{x}_2, \dots, \mathbf{x}_M\} \in \mathbb{Z}^{M \times 3}$ . The voxelization process can be described as follows:

$$\tilde{\mathbf{x}}_n = \text{floor}(\mathbf{x}_n^{\text{pt}}/l) \quad \text{for } \mathbf{x}_n^{\text{pt}} \in \mathcal{X}^{\text{pt}} \quad (21)$$

$$\{\tilde{\mathbf{x}}_n\}_{n \in \mathcal{I}} = \text{unique}(\{\tilde{\mathbf{x}}_n\}_{n=1}^N) \quad (22)$$

$$\{\mathbf{x}_m\}_{m=1}^M = \{\tilde{\mathbf{x}}_n\}_{n \in \mathcal{I}} \quad (23)$$

where  $l$  is the voxel size, and indices  $\mathcal{I}$  is a subset of  $\{n\}_{n=1}^N$  that satisfies  $|\mathcal{I}| = M$ . The voxel size is unified as 1 in  $\mathcal{X}$  after voxelization.

**3D Sparse Convolution.** We consider a sparse convolution kernel with weights  $\mathbf{W} \in \mathbb{R}^{C \times D' \times D}$  and a bias  $\mathbf{b} \in \mathbb{R}^{D'}$  that

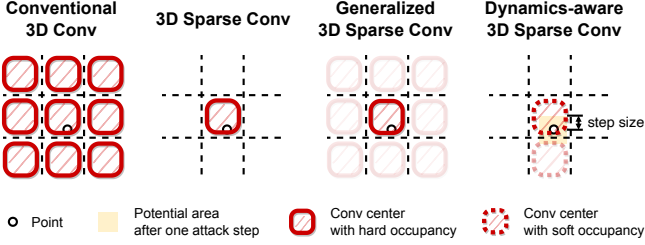


Fig. 5. An illustration of conventional 3D convolution that operates on every voxels, 3D sparse convolution in (24), generalized 3D sparse convolution in (25), and our dynamics-aware 3D sparse convolution in (27) with soft occupancy in (31). We only draw the convolution center in this figure for concise, and the color shade indicates the magnitude of the convolution's occupancy value.

operates on a voxel coordinate  $\mathbf{x}_m \in \mathcal{X}$ . The weights  $\mathbf{W}$  can be broken down into spatial weights  $W_{\mathbf{u}}$  with  $C$  matrices of size  $D' \times D$ , where  $\mathbf{u} \in \mathbb{Z}^3$  is a coordinate offset belonging to  $\mathcal{S} \in \mathbb{Z}^{C \times 3}$ . We define the features of current sparse voxels as  $\{\mathbf{f}_1, \mathbf{f}_2, \dots, \mathbf{f}_M\} \in \mathbb{R}^{M \times D}$ . The convolution output feature  $\mathbf{f}'_m \in \mathbb{R}^{D'}$  of the  $m$ -th voxel is derived as:

$$\mathbf{f}'_m = \sum_{\mathbf{x}_q \in \mathcal{K}(\mathbf{x}_m, \mathcal{X}, \mathcal{S})} W_{\mathbf{x}_q - \mathbf{x}_m} \mathbf{f}_q + \mathbf{b} \quad \text{for } \mathbf{x}_m \in \mathcal{X}, \quad (24)$$

where  $\mathcal{K}(\mathbf{x}_m, \mathcal{X}, \mathcal{S}) = \{\mathbf{x}_q | \mathbf{x}_q = \mathbf{x}_m + \mathbf{u} \in \mathcal{X}, \mathbf{x}_q \in \mathcal{X}, \mathbf{u} \in \mathcal{S}\}$  is a collection of sparse voxel coordinates in  $\mathcal{X}$  that covered by the kernel shape centered at  $\mathbf{x}_m$ .

**FGM in 3D Sparse Convolution.** Similar to the formula in (2), we introduce a constant occupancy value  $\bar{o} \in \{0, 1\}$  to show whether an arbitrary voxel coordinate  $\mathbf{x} \in \mathbb{Z}^3$  belongs to the current sparse voxel set  $\mathcal{X}$ . Therefore, we can release 3D sparse convolution in (24) into generalized 3D sparse convolution that operates on every voxel in the 3D grid regardless of whether the voxel contains point(s). The two kinds of convolutions share the same weights, and they behave the same when the voxel is valid, i.e.  $\bar{o} = 1$ . In this case, (24) becomes:

$$\mathbf{f}'_{\text{FGM}} = \bar{o} \cdot \left( \sum_{\mathbf{x}_q \in \mathcal{K}(\mathbf{x}, \mathcal{X}, \mathcal{S})} W_{\mathbf{x}_q - \mathbf{x}} \mathbf{f}_q + \mathbf{b} \right). \quad (25)$$

When calculating gradients of an existence voxel  $\mathbf{x}$  without consideration of the potential changes of sparse convolution, the partial derivative of  $\mathbf{f}'_{\text{FGM}}$  with respect to a point  $\mathbf{x}_n^{\text{pt}} \in \mathcal{X}^{\text{pt}}$  is:

$$\frac{\partial \mathbf{f}'_{\text{FGM}}}{\partial \mathbf{x}_n^{\text{pt}}} = \bar{o} \cdot \left( \sum_{\mathbf{x}_q \in \mathcal{K}(\mathbf{x}, \mathcal{X}, \mathcal{S})} W_{\mathbf{x}_q - \mathbf{x}} \frac{\partial \mathbf{f}_q}{\partial \mathbf{x}_n^{\text{pt}}} \right). \quad (26)$$

**LGM in 3D Sparse Convolution.** According to the definition of 3D sparse convolution, it only conducts on existing voxels  $\mathcal{X}$ . If the voxel  $\mathbf{x}_m$  does not contain point(s) and disappears after one attack step, the convolution on voxel  $\mathbf{x}_m$  becomes invalid. This change in network architecture causes the learned perturbation may not be efficient to the changed new architecture. To be aware of the dynamic location of sparse convolution, we consider the changes of the occupancy values  $o(\mathbf{x}, \mathcal{X})$  along with the perturbations on the input. We

present a dynamics-aware 3D sparse convolution and rewrite (25) as:

$$\mathbf{f}'_{\text{LGM}} = o(\mathbf{x}, \mathcal{X}) \cdot \left( \sum_{\mathbf{x}_q \in \mathcal{K}(\mathbf{x}, \mathcal{X}, \mathcal{S})} W_{\mathbf{x}_q - \mathbf{x}} \mathbf{f}_q + \mathbf{b} \right). \quad (27)$$

Although  $\mathbf{f}'_{\text{FGM}}$  and  $\mathbf{f}'_{\text{LGM}}$  in (25) and (27) are the same in value, the formulas of gradient calculation are different. The partial derivative of  $\mathbf{f}'_{\text{LGM}}$  in (27) with respect to a point  $\mathbf{x}_n^{\text{pt}} \in \mathcal{X}^{\text{pt}}$  is:

$$\begin{aligned} \frac{\partial \mathbf{f}'_{\text{LGM}}}{\partial \mathbf{x}_n^{\text{pt}}} = & \bar{o} \cdot \left( \sum_{\mathbf{x}_q \in \mathcal{K}(\mathbf{x}, \mathcal{X}, \mathcal{S})} W_{\mathbf{x}_q - \mathbf{x}} \frac{\partial \mathbf{f}_q}{\partial \mathbf{x}_n^{\text{pt}}} \right) \\ & + \frac{\partial o(\mathbf{x}, \mathcal{X})}{\partial \mathbf{x}_n^{\text{pt}}} \cdot \left( \sum_{\mathbf{x}_q \in \mathcal{K}(\mathbf{x}, \mathcal{X}, \mathcal{S})} W_{\mathbf{x}_q - \mathbf{x}} \mathbf{f}_q + \mathbf{b} \right). \end{aligned} \quad (28)$$

Compared with traditional fast gradient calculation that does not consider dynamic architecture changes in (26), we can discover that (28) has one more derivative on  $\frac{\partial o(\mathbf{x}, \mathcal{X})}{\partial \mathbf{x}_n^{\text{pt}}}$ , which ensures the existence change of convolution is reflected in the back-propagated gradients. Fig. 5 illustrates the difference between sparse convolution, generalized sparse convolution, and our dynamics-aware sparse convolution. The figure is presented in the 2D view.

**Non-differentiable Function Approximation.** To calculate the derivative  $\frac{\partial o(\mathbf{x}, \mathcal{X})}{\partial \mathbf{x}_n^{\text{pt}}}$ , it can be released by  $\frac{\partial o(\mathbf{x}, \mathcal{X})}{\partial \mathbf{x}} \frac{\partial \mathbf{x}}{\partial \mathbf{x}_n^{\text{pt}}}$ . However, due to the binary definition of  $o(\mathbf{x}, \mathcal{X}) \in \{0, 1\}$  and the non-differentiable voxelization process in (21-23), the derivative  $\frac{\partial o(\mathbf{x}, \mathcal{X})}{\partial \mathbf{x}}$  and  $\frac{\partial \mathbf{x}}{\partial \mathbf{x}_n^{\text{pt}}}$  are both not everywhere differentiable in the domain of definition, leading to the received gradient valueless. Following BPDA [53], we choose to reformulate the hard occupancy  $o(\mathbf{x}, \mathcal{X})$  into a differentiable soft occupancy  $\hat{o}(\mathbf{x}, \mathcal{X}^{\text{pt}}) \approx o(\mathbf{x}, \mathcal{X})$  that directly requires point coordinates as input. To model the soft occupancy function  $\hat{o}(\mathbf{x}, \mathcal{X}^{\text{pt}})$ , we consider the occupancy value of an arbitrary voxel  $\mathbf{x}$  in 3D space is essentially determined by a conditional statement: “If at least one point in the point cloud belongs to the voxel, then the occupancy value is 1, and otherwise 0.” This process can be split into two stages:

- 1) Obtain a relation value  $r(\mathbf{x}, \mathbf{x}_n^{\text{pt}}) \in \{0, 1\}$  to show the existence of the point  $\mathbf{x}_n^{\text{pt}}$  in the given voxel  $\mathbf{x}$ .
- 2) Gather all the relation values for the given voxel  $\mathbf{x}$  together and find whether 1 exists. If at least one relation value equals 1, then the occupancy value of the given voxel is 1, and otherwise 0.

Because both the two stages are not everywhere differentiable, we need to find functions to approximate them.

For the first stage, we present a differentiable function  $\hat{r}(\mathbf{x}, \mathbf{x}_n^{\text{pt}}) \in (0, 1)$  to replace  $r(\mathbf{x}, \mathbf{x}_n^{\text{pt}}) \in \{0, 1\}$  for occupancy calculation. When the point  $\mathbf{x}_n^{\text{pt}}$  is nearer to the center of the voxel  $\mathbf{x}$ , we let the output relation value be higher and closer to 1. Some functions have been proposed to solve the non-differentiable problem in voxel occupancy, like bilinear interpolation [64] and radial basis function [65]. In this paper, we construct a sigmoid-like function and find it more suitable

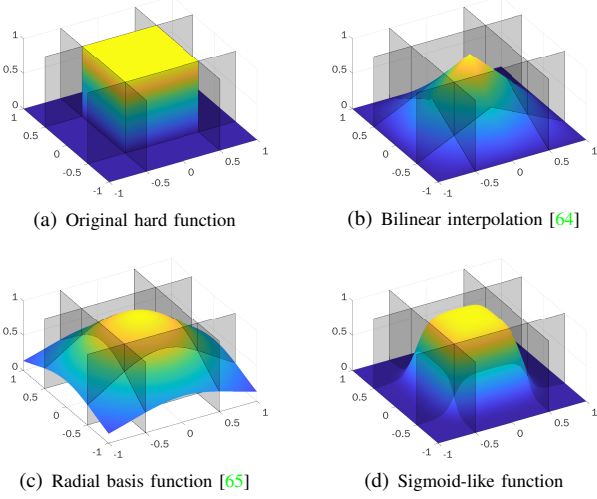


Fig. 6. The visualization results on various relation functions. The gray planes show the voxel boundaries. Our sigmoid-like function well approximates the original function and has nice gradient quality near the voxel boundaries.

in attacks on 3D voxel-based networks. The differentiable relation function  $\hat{r}(\mathbf{x}, \mathbf{x}_n^{\text{pt}})$  is as follows:

$$d(\mathbf{x}, \mathbf{x}_n^{\text{pt}}) = |(\mathbf{x} + 0.5) - \mathbf{x}_n^{\text{pt}}/L|, \quad (29)$$

$$\hat{r}(\mathbf{x}, \mathbf{x}_n^{\text{pt}}) = \prod_{i \in \{0,1,2\}} \frac{1}{1 + \exp(\lambda \cdot (d(\mathbf{x}, \mathbf{x}_n^{\text{pt}})_i - 0.5))}, \quad (30)$$

where  $d(\mathbf{x}, \mathbf{x}_n^{\text{pt}}) \in \mathbb{R}^3$  outputs a distance vector,  $L$  is the voxel size,  $d(\mathbf{x}, \mathbf{x}_n^{\text{pt}})_i$  represents the  $i$ -th element of  $d(\mathbf{x}, \mathbf{x}_n^{\text{pt}})$ , and  $\lambda$  is a parameter that controls the slope near the voxel boundary. Fig. 6 shows the visualization results of original hard function, bilinear interpolation [64], radial basis function [65], and our sigmoid-like function. Compared to the existing two functions, our sigmoid-like function is more similar to the original hard function and has more significant gradient variation near voxel boundaries. When a point locates near the voxel boundary, the gradient will become distinctly large to force the point to quickly move in/out of the voxel, instead of staying near the boundary. We also conduct experiments on these functions and demonstrate the superior of our sigmoid-like function.

For the second stage, we consider the gathering as an “or” operation in nature and present a differentiable function  $g(\cdot)$  for this operation. Finally, our reformulated  $\hat{o}(\mathbf{x}, \mathcal{X}^{\text{pt}})$  is derived as follows:

$$\begin{aligned} \hat{o}(\mathbf{x}, \mathcal{X}^{\text{pt}}) &= g(\{\hat{r}(\mathbf{x}, \mathbf{x}_n^{\text{pt}}) \mid \mathbf{x}_n^{\text{pt}} \in \mathcal{N}(\mathbf{x}, \mathcal{X}^{\text{pt}})\}) \\ &= 1 - \prod_{\mathbf{x}_n^{\text{pt}} \in \mathcal{N}(\mathbf{x}, \mathcal{X}^{\text{pt}})} (1 - \hat{r}(\mathbf{x}, \mathbf{x}_n^{\text{pt}})), \end{aligned} \quad (31)$$

where  $\mathcal{N}(\mathbf{x}, \mathcal{X}^{\text{pt}})$  is a subset of point cloud  $\mathcal{X}^{\text{pt}}$  to reduce the huge computational costs. For a given voxel  $\mathbf{x}$ , we only gather the relation values of those points that possibly exist in the voxel after one attack step. If a voxel has no points to gather values, the voxel is ignored throughout the network. Therefore, we actually extend existing  $M$  sparse voxels into  $M'$  voxels, by adding a number of surrounding empty voxels that are possibly valid after one attack step. In our implementations, the step size at each iteration to perturb the point cloud coordinates is set very small for better optimizing

performance. We find  $M' \approx 1.5M$ , so the computational cost of our extended convolutions is tolerable. By multiplying the specially designed occupancy function on every convolution, we can obtain a leaded gradient that is aware of the dynamic network architecture.

## V. EXPERIMENTS ON 2D IMAGE ATTACK

In this section, we evaluate our proposed dynamics-aware attack on layer skipping network and 2D sparse convolution network on 2D image datasets and analyze their performance against baseline dynamics-unaware methods.

### A. Datasets and Implementation Details

We conduct experiments on two popular image datasets: CIFAR-10 [8] and ImageNet [9].

We adopt SkipNet [5] for layer skipping network and DynConv [6] for 2D sparse convolution network. In the experiments of CIFAR-10, the network backbone is ResNet-110 [33] for SkipNet and ResNet-32 [33] for DynConv. We also provide attack results on the normally trained static ResNet-110 and ResNet-32 for reference. On the ImageNet dataset, SkipNet and DynConv both adopt the network backbone ResNet-101 [33] in their work, which enables us to fairly compare the attack performance between dynamically changing the network architecture layer-wise and within the layer. We also provide attack results on the normally trained static ResNet-101 for reference.

We perform our FGM and LGM on the basic attack algorithms FGSM [2] and I-FGSM [14] to show the primitive attack performance difference between FGM and LGM in a single attack step and multiple attack steps. We constrain the maximum perturbation magnitude  $\epsilon$  in  $L_\infty$  norm. For I-FGSM, we follow [14] to set the number of iteration as  $\min(\epsilon + 4, 1.25\epsilon)$ . For LGM, we set  $\lambda$  for the sigmoid function in (15) in range  $0.0001 \sim 40$  for different attack settings. We find that given a large attack step  $\alpha$ , such as  $\alpha = 16$  in the single step attack FGSM, when the  $\lambda$  is small our LGM performs the best.

### B. Results and Analysis

Tables I and II show the attack results on the CIFAR-10 [8] and ImageNet [9] datasets in different maximum perturbation magnitudes  $\epsilon$ . “Bf. Attack” is “Before Attack” for short. “Valid Pxl.” is “Valid Pixel” for short, which denotes the percentage of attacked pixels in all pixels of the image. On all datasets with all  $\epsilon$ , our LGM significantly outperforms the dynamics-unaware FGM, which fully validates the importance of the attack method to be aware of the dynamic architecture changes. In the FGSM [2] attack, the advantage of LGM is more apparent when  $\epsilon \geq 2$ , which gives strong evidence of the superiority of our LGM. Since I-FGSM [14] attack can successfully attack all images when all pixels are perturbed, we restrict the percentage of pixels in attack and find our LGM also superior to the dynamics-unaware FGM.

To evaluate the magnitude of network architecture change during the attack, we calculate the architecture change ratio

TABLE I  
IMAGE CLASSIFICATION RESULTS (%) ON THE CIFAR-10 TESTING SET IN DIFFERENT  $\epsilon$  (M) FOR VARIOUS MODELS AND METHODS.

| Method                | Valid PxL. | SkipNet (ResNet-110) |             |              |             | ResNet-110<br>FGM | DynConv (ResNet-32) |             |              |             | ResNet-32<br>FGM |
|-----------------------|------------|----------------------|-------------|--------------|-------------|-------------------|---------------------|-------------|--------------|-------------|------------------|
|                       |            | FGM                  | Archi. Chg. | LGM          | Archi. Chg. |                   | FGM                 | Archi. Chg. | LGM          | Archi. Chg. |                  |
| Bf. Attack            | -          | 93.30                |             |              |             | 93.68             | 93.05               |             |              |             | 92.63            |
| FGSM $\epsilon = 1$   | 100%       | 26.70                | 4.64        | <b>25.52</b> | 4.47        | 36.00             | 42.11               | 1.75        | <b>39.54</b> | 1.76        | 31.33            |
| FGSM $\epsilon = 2$   | 100%       | 16.67                | 8.04        | <b>12.23</b> | 8.17        | 25.77             | 30.63               | 2.71        | <b>18.13</b> | 2.7         | 21.45            |
| FGSM $\epsilon = 4$   | 100%       | 11.76                | 12.16       | <b>6.52</b>  | 12.68       | 20.61             | 22.92               | 3.87        | <b>6.57</b>  | 3.87        | 16.76            |
| FGSM $\epsilon = 8$   | 100%       | 9.69                 | 17.18       | <b>6.71</b>  | 17.26       | 16.03             | 14.08               | 5.36        | <b>5.05</b>  | 5.27        | 12.01            |
| I-FGSM $\epsilon = 8$ | 100%       | 0.00                 | 11.99       | 0.00         | 10.99       | 0.00              | 0.00                | 3.87        | 0.00         | 4.03        | 0.00             |
| I-FGSM $\epsilon = 8$ | 20%        | 1.30                 | 6.45        | <b>1.26</b>  | 6.01        | 1.78              | 4.62                | 2.18        | <b>4.58</b>  | 2.21        | 0.78             |
| I-FGSM $\epsilon = 8$ | 10%        | 18.68                | 4.18        | <b>18.41</b> | 3.94        | 21.26             | 28.87               | 1.51        | <b>28.16</b> | 1.52        | 16.77            |
| I-FGSM $\epsilon = 8$ | 5%         | 50.64                | 2.57        | <b>49.95</b> | 2.33        | 54.11             | 57.75               | 0.94        | <b>56.82</b> | 0.93        | 49.21            |

TABLE II  
IMAGE CLASSIFICATION RESULTS (%) ON THE IMAGENET VALIDATION SET IN DIFFERENT  $\epsilon$  (M) FOR VARIOUS MODELS AND METHODS.

| Method                 | Valid PxL. | SkipNet (ResNet-101) |             |              |             | FGM   | DynConv (ResNet-101) |              |       |             | ResNet-101<br>FGM |
|------------------------|------------|----------------------|-------------|--------------|-------------|-------|----------------------|--------------|-------|-------------|-------------------|
|                        |            | FGM                  | Archi. Chg. | LGM          | Archi. Chg. |       | FGM                  | Archi. Chg.  | LGM   | Archi. Chg. |                   |
| Bf. Attack             | -          | 77.02                |             |              |             | 76.85 |                      |              |       | 77.31       |                   |
| FGSM $\epsilon = 1$    | 100%       | 10.14                | 3.15        | <b>10.09</b> | 3.42        | 11.69 | 2.65                 | <b>11.31</b> | 2.77  | 9.29        |                   |
| FGSM $\epsilon = 2$    | 100%       | 9.45                 | 4.39        | <b>6.82</b>  | 4.63        | 10.20 | 3.89                 | <b>7.84</b>  | 4.13  | 8.39        |                   |
| FGSM $\epsilon = 4$    | 100%       | 11.61                | 5.87        | <b>5.35</b>  | 6.08        | 11.60 | 5.53                 | <b>4.52</b>  | 5.82  | 10.14       |                   |
| FGSM $\epsilon = 8$    | 100%       | 15.33                | 7.86        | <b>5.25</b>  | 8.10        | 14.37 | 7.37                 | <b>3.36</b>  | 7.66  | 12.89       |                   |
| FGSM $\epsilon = 16$   | 100%       | 12.28                | 10.81       | <b>4.28</b>  | 10.92       | 11.31 | 9.71                 | <b>2.54</b>  | 10.02 | 9.67        |                   |
| I-FGSM $\epsilon = 16$ | 100%       | 0.00                 | 8.36        | 0.00         | 5.83        | 0.00  | 6.82                 | 0.00         | 7.28  | 0.00        |                   |
| I-FGSM $\epsilon = 16$ | 2%         | 6.22                 | 2.08        | <b>6.16</b>  | 1.34        | 10.60 | 2.24                 | <b>10.57</b> | 1.99  | 6.51        |                   |
| I-FGSM $\epsilon = 16$ | 1%         | 23.20                | 1.56        | <b>22.96</b> | 1.11        | 30.66 | 1.71                 | <b>29.78</b> | 1.50  | 24.99       |                   |
| I-FGSM $\epsilon = 16$ | 0.5%       | 45.64                | 1.12        | <b>45.14</b> | 0.91        | 51.13 | 1.23                 | <b>50.36</b> | 1.09  | 47.37       |                   |

as the number of changed computation units after the attack divided by the number of all changeable computation units. For the layer skipping network SkipNet [5], the architecture is changed layer-wise and the number of changeable layers is 53 for ResNet-110 and 32 for ResNet-101. For the 2D sparse convolution network DynConv [6], the architecture is changed pixel-wise and the number of changeable pixels is the sum of the pixel number of the input image and all inner feature maps. In Tables I and II, we list the architecture change ratio (%) as “Archi. Chg.”. We find that our LGM tends to change more computation units in FGSM [2] attack, but change fewer computation units in I-FGSM attack [14]. We initially thought that our LGM may tend to change more computation units to cause chaos in the architecture in order to misclassify the input image, but the results show that whether to change a computation unit should be appropriately based on its status.

Because the layer skipping network and 2D sparse convolution network deactivate unnecessary computation units in the static neural networks, we also compare their robustness against their corresponding static neural networks. We show the attack performance on ResNet-110 and ResNet-32 in Table I for the CIFAR-10 dataset, and ResNet-101 in Table II for the ImageNet dataset. When adopting dynamics-unaware FGM in attack, the results reveal that the layer skipping network SkipNet [5] is less robust than its corresponding static neural network, while the 2D sparse convolution network DynConv [6] shows better robustness. When adopting LGM in the FGSM [2] attack with  $\epsilon \geq 2$ , the adaptive neural networks are all easier to be attacked than static neural networks.

We also analyze the layer-wise activation behavior in the layer skipping network SkipNet [5] before and after the attack. In Fig. 7 (top), we follow [66] to show the rates at which different layers are executed (x-axis) for images of the 1000 classes in ImageNet (y-axis). The number of changeable layers is 32. “GT Classes” denotes the images presented as their ground-truth classes, and “Attacked Classes” denotes the images presented as their misclassified classes. We also show the mid-level categories on the y-axis for clarity. In Fig. 7 (bottom), we present the PCA results of the layer execution rates. Combining the histogram and PCA results before attack in Fig. 7 (a), we observe a clear difference between layers used for man-made objects (*food, consumer goods, container, equipment, structures, transport, and other objects*) and for animals (*birds, dogs, other mammals, reptiles, and other animals*). We also find some mid-level categories have distinct differences in both the histogram and PCA results, such as *birds, dogs, food, and transport*. When the attack is finished in Figs. 7 (b) and (d), we find that the layer-wise behaviors tend to be the same. In the histograms of Figs. 7 (c) and (e), the white lines denote the images in these classes are all successfully attacked. Compared to FGM, LGM can force more classes to be successfully attacked. For the PCA results in Figs. 7 (b-e), we can also find a clear difference between man-made objects and animals. The layer-wise behavior of mid-classes reveals that the layers can be selectively activated based on the semantic class of the input image. The semantic behavior of layers can also be kept to a certain degree after the attack.

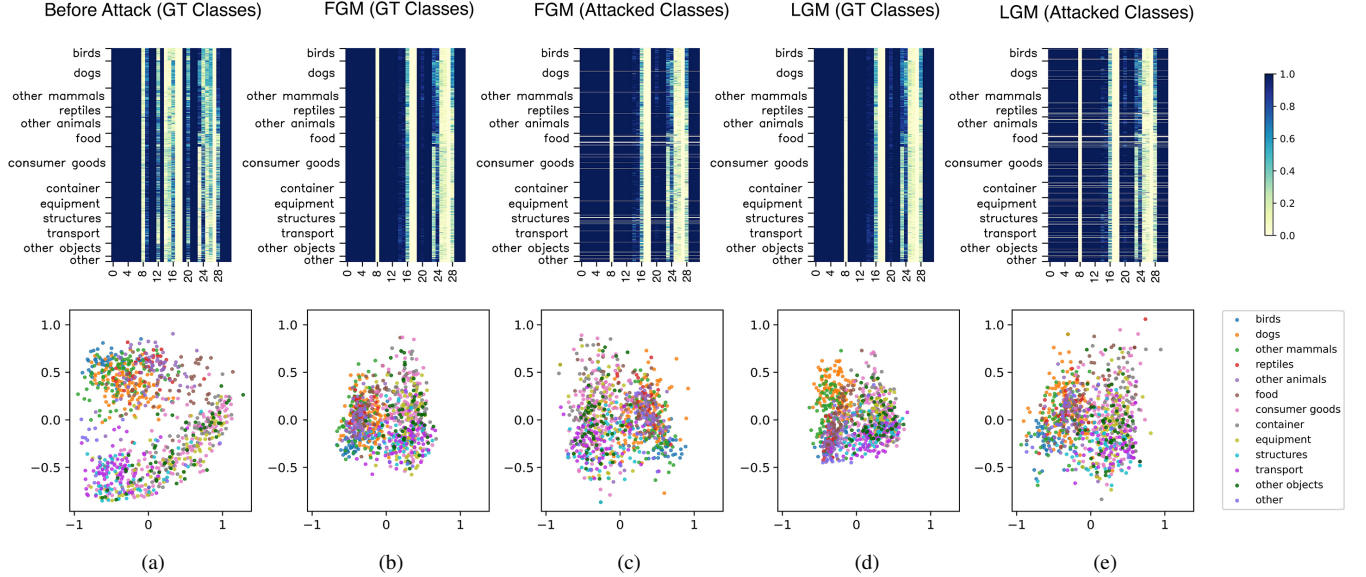


Fig. 7. The visualization results of layer-wise behavior in the layer skipping network before and after the attack on the ImageNet validation set. We conduct the FGSM attack with maximum perturbation  $\epsilon = 16$ .

## VI. EXPERIMENTS ON 3D POINT CLOUD ATTACK

In this section, we evaluate our proposed dynamics-aware attack on 3D sparse convolution network on 3D point cloud datasets and analyze its performance against baseline dynamics-unaware methods.

### A. Datasets and Implementation Details

We conduct experiments on three popular point cloud datasets, including two indoor scene datasets ScanNet [10], S3DIS [11], [12], and an outdoor scene dataset SemanticKITTI [13].

We adopt MinkowskiNet [45] on the ScanNet and S3DIS datasets, and Cylinder3D [46] on the SemanticKITTI dataset for semantic segmentation. The two network architectures are both built on the base of 3D sparse convolution [7] and achieve state-of-the-art performance.

To attack the network, we compute a cross-entropy loss for gradient back-propagation. We adopt our FGM and LGM based on a variant version of I-FGSM [14] proposed by Liu *et al.* [22] that tailors the real number nature of point cloud coordinates. We constrain the maximum perturbation magnitude  $\epsilon$  for each point onto the surface of a 3D cube by  $L_\infty$  norm. The unit of  $\epsilon$  is meter. We traverse different attack step size  $\alpha$  in range  $0.0005 \sim 0.025$  and different  $\lambda$  for the sigmoid-like function (30) in range  $10 \sim 55$  to adopt their best one for different  $\epsilon$ . The iteration number for the ScanNet and S3DIS datasets is 50, and for the SemanticKITTI dataset is 30.

### B. Results and Analysis

Tables III-V show the attack results on the ScanNet [10], S3DIS [11], [12], and SemanticKITTI [13] datasets in different maximum perturbation magnitudes  $\epsilon$ . “Bf. Attack” is “Before Attack” for short. On all datasets with all  $\epsilon$ , our LGM significantly outperforms the dynamics-unaware FGM

TABLE III  
POINT CLOUD SEMANTIC SEGMENTATION MIoU RESULTS (%) ON THE SCANNET VALIDATION SET IN DIFFERENT  $\epsilon$  (M) FOR VARIOUS METHODS.

| Method     | $\epsilon = 0.005$ | $\epsilon = 0.01$ | $\epsilon = 0.02$ | $\epsilon = 0.05$ |
|------------|--------------------|-------------------|-------------------|-------------------|
| Bf. Attack | 72.22              |                   |                   |                   |
| Random     | 71.22              | 70.07             | 57.30             | 15.58             |
| FGM        | 60.44              | 55.51             | 38.65             | 8.70              |
| LGM        | <b>25.79</b>       | <b>11.51</b>      | <b>5.76</b>       | <b>3.83</b>       |

TABLE IV  
POINT CLOUD SEMANTIC SEGMENTATION MIoU RESULTS (%) ON THE S3DIS AREA 5 IN DIFFERENT  $\epsilon$  (M) FOR VARIOUS METHODS.

| Method     | $\epsilon = 0.005$ | $\epsilon = 0.01$ | $\epsilon = 0.02$ | $\epsilon = 0.05$ |
|------------|--------------------|-------------------|-------------------|-------------------|
| Bf. Attack | 66.35              |                   |                   |                   |
| Random     | 61.35              | 58.50             | 52.17             | 23.90             |
| FGM        | 57.53              | 52.35             | 45.24             | 21.21             |
| LGM        | <b>48.20</b>       | <b>39.65</b>      | <b>30.93</b>      | <b>7.45</b>       |

and random perturbation, which fully validates the importance of the attack method to be aware of the dynamic architecture changes. On the ScanNet and S3DIS datasets, we find the performance drop from FGM to LGM is about twice as much as the drop from random perturbation to FGM. In contrast, the performance drop for LGM on the SemanticKITTI dataset is not as good as the ScanNet and S3DIS datasets. This phenomenon can be explained by the fact that the point cloud coordinates of the SemanticKITTI dataset are included in point features, while the point features of the ScanNet and S3DIS datasets only contain RGB colors. With the included point cloud coordinates, the gradient back-propagation pass has better quality than those point cloud features that do not include coordinates. Therefore, the impact of dynamic architecture becomes less impressive in the context of a better

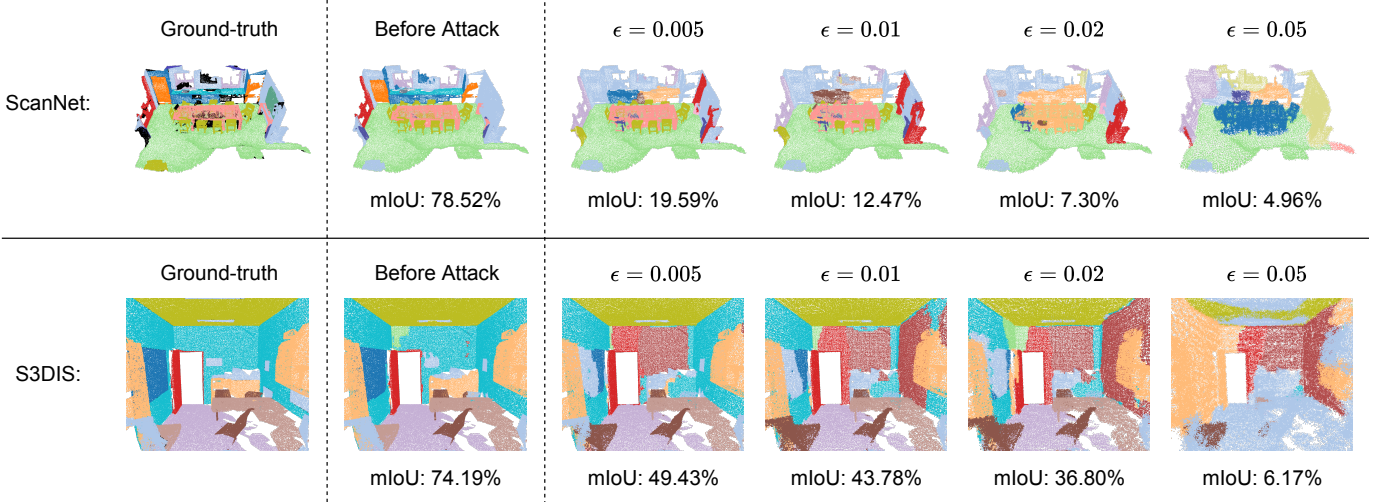


Fig. 8. The qualitative visualization results of LGM on the ScanNet validation set and S3DIS area 5 in different  $\epsilon$  (m). The black areas in ground-truth are unlabeled.

TABLE V

POINT CLOUD SEMANTIC SEGMENTATION MIOU RESULTS (%) ON THE SEMANTICKITTI VALIDATION SET IN DIFFERENT  $\epsilon$  (M) FOR VARIOUS METHODS.

| Method     | $\epsilon = 0.01$ | $\epsilon = 0.02$ | $\epsilon = 0.05$ | $\epsilon = 0.1$ |
|------------|-------------------|-------------------|-------------------|------------------|
| Bf. Attack | 66.91             |                   |                   |                  |
| Random     | 64.71             | 50.46             | 18.68             | 8.74             |
| FGM        | 36.93             | 25.61             | 10.94             | 5.26             |
| LGM        | <b>31.16</b>      | <b>19.93</b>      | <b>7.28</b>       | <b>3.96</b>      |

gradient pass in features.

The results also reveal that there is a distinct performance drop when  $\epsilon$  is close to the voxel size of 0.02 m for the ScanNet dataset and 0.05 m for the S3DIS dataset. When  $\epsilon$  equals the voxel size, all points within a voxel can move out of the voxel and their potential destinations cover not only their currently belonging voxel but all surrounding 26 voxels in 3D space. This phenomenon may not be obvious on the SemanticKITTI dataset, since the Cylinder3D network voxelizes the point cloud in cylindrical-coordinate system with cylinder partition size ( $0.1$  m,  $\frac{1}{2\pi}$ ,  $0.19$  m) for  $(\rho, \theta, z)$ .

Figs. 8-9 show the visualization results of our dynamics-aware LGM on the ScanNet, S3DIS, and SemanticKITTI datasets. We observe that the perturbed point cloud coordinates are imperceptible to human eyes in some small  $\epsilon$ , such as  $\epsilon = 0.005$  m (0.5 cm) and  $\epsilon = 0.01$  m (1 cm) on the ScanNet and S3DIS datasets and  $\epsilon = 0.01$  m (1 cm) and  $\epsilon = 0.02$  m (2 cm) on the SemanticKITTI dataset, but these maximum perturbations do cause significant wrong predictions of the victim networks. This huge contrast reveals a great security risk in real-world applications of 3D sparse convolution networks.

We also present class-specific semantic IoUs on the ScanNet dataset in Table VI to show the vulnerability of each class. The results show that other than the class *floor* most classes are easy to attack, which is consistent with the visualization results in Fig. 8. The class *wall*, *bed*, *chair*, *toilet* and *bathtub* also have a certain degree of robustness. This may be explained by the fact that these robust classes have discriminative characteristics in their global shapes or locations, therefore they are

difficult to be destroyed through local point perturbation by attacks.

We also conduct attacks that utilize different soft occupancy functions  $\hat{o}(\mathbf{x}, \mathcal{X}^{\text{PT}})$ , including bilinear interpolation (BI) [64], radial basis function (RBF) [65], and our sigmoid-like function in (30). Table VII shows the attack performance on the ScanNet validation set in different  $\epsilon$ . The results validate the effectiveness of our sigmoid-like function (denoted as Sigmoid). Compared to the visualized functions in Fig. 6, we find that our sigmoid-like function imitates the hard occupancy better than RBF and BI, and their attack results in Table VII are consistent with their imitation qualities.

## VII. CONCLUSION

In this paper, we have investigated the lagged gradient issue in adversarial attacks for adaptive neural networks that have dynamic architecture and we have proposed a Leaded Gradient Method (LGM) for the dynamics-aware adversarial attack. We take layer skipping network and 2D/3D sparse convolution network as typical examples of adaptive neural networks to design our method. Specifically, we first analyze the missing part in traditional gradient calculation that considers the architecture changes. We then reformulate the gradient to better “lead” each attack step. Experimental results on both 2D images and 3D point clouds show our LGM achieves impressive performance and outperforms dynamics-unaware baseline methods. We believe our dynamics-aware attack can be used for other adaptive neural networks.

## VIII. ACKNOWLEDGEMENT

This work was supported in part by the National Natural Science Foundation of China under Grant 62125603, Grant U1813218, and Grant 62206147, and in part by a grant from the Beijing Academy of Artificial Intelligence (BAAI). We thank He Wang, Ziyi Wu, Pengliang Ji, and Haowen Sun for their valuable supports on algorithms and experiments of adversarial attack against 3D sparse convolution networks.

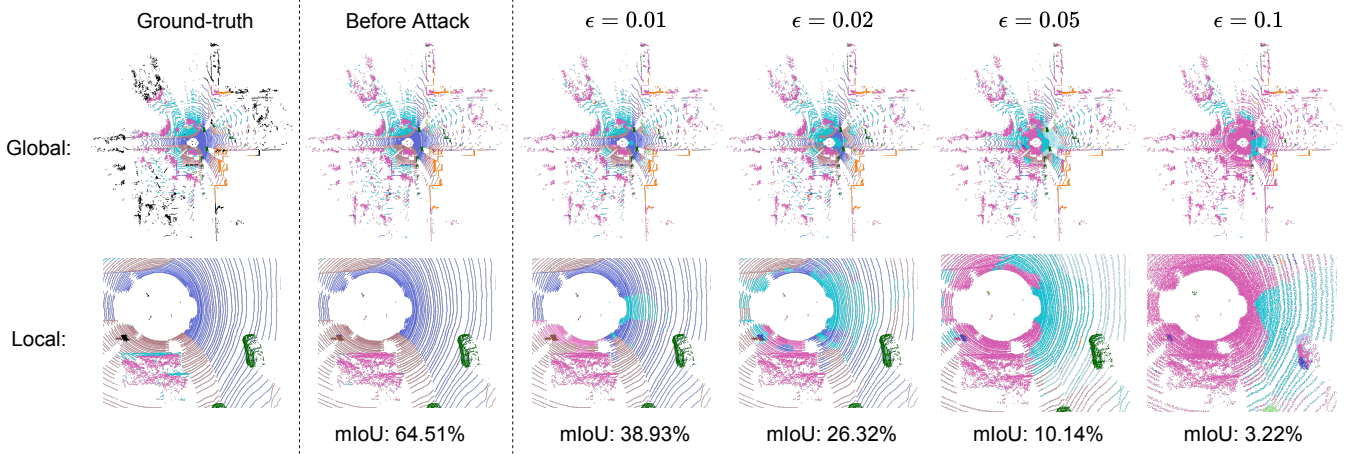


Fig. 9. The qualitative visualization results of LGM on the SemanticKITTI validation set in different  $\epsilon$  (m). The scene is presented in both a global view and a local view. The black areas in ground-truth are ignored labels.

TABLE VI  
THE CLASS-SPECIFIC SEMANTIC IOUs (%) ON THE SCANNET VALIDATION SET IN  $\epsilon = 0.01$  FOR VARIOUS METHODS.

| Method     | Wall        | Floor       | Cab        | Bed        | Chair       | Sofa        | Table       | Door       | Wind.      | Bshf.      | Pic.       | Cntr.      | Desk       | Curt.      | Fridg.     | Shwr.      | Toil.       | Sink       | Bath.       | Ofrun.     | Mean        |
|------------|-------------|-------------|------------|------------|-------------|-------------|-------------|------------|------------|------------|------------|------------|------------|------------|------------|------------|-------------|------------|-------------|------------|-------------|
| Bf. Attack | 83.3        | 94.8        | 66.0       | 80.1       | 91.2        | 81.7        | 76.3        | 61.4       | 59.1       | 80.7       | 29.5       | 63.3       | 64.3       | 75.9       | 62.1       | 69.2       | 92.1        | 66.8       | 85.9        | 60.0       | 72.2        |
| Random     | 81.7        | 94.1        | 63.5       | 79.0       | 90.3        | 82.5        | 72.9        | 56.2       | 57.0       | 79.5       | 26.0       | 61.4       | 61.9       | 73.7       | 57.2       | 67.3       | 91.6        | 64.6       | 84.8        | 56.1       | 70.1        |
| FGM        | 70.1        | 92.6        | 45.9       | 73.7       | 84.0        | 71.9        | 55.7        | 33.5       | 37.2       | 58.1       | 12.5       | 46.7       | 37.9       | 58.0       | 35.9       | 47.5       | 80.6        | 55.0       | 77.2        | 36.4       | 55.5        |
| LGM        | <b>10.8</b> | <b>85.6</b> | <b>5.8</b> | <b>7.7</b> | <b>26.5</b> | <b>10.7</b> | <b>11.8</b> | <b>2.9</b> | <b>2.9</b> | <b>1.1</b> | <b>0.7</b> | <b>0.4</b> | <b>3.6</b> | <b>1.6</b> | <b>0.0</b> | <b>4.0</b> | <b>23.3</b> | <b>7.0</b> | <b>22.7</b> | <b>1.4</b> | <b>11.5</b> |

TABLE VII

POINT CLOUD SEMANTIC SEGMENTATION MIOU RESULTS (%) ON THE SCANNET VALIDATION SET IN DIFFERENT  $\epsilon$  (M) FOR VARIOUS OCCUPANCY FUNCTIONS.

| Method     | $\epsilon = 0.005$ | $\epsilon = 0.01$ | $\epsilon = 0.02$ | $\epsilon = 0.05$ |
|------------|--------------------|-------------------|-------------------|-------------------|
| Bf. Attack |                    | 72.22             |                   |                   |
| BI [64]    | 68.08              | 60.21             | 32.62             | 11.73             |
| RBF [65]   | 36.14              | 16.62             | 8.29              | 5.00              |
| Sigmoid    | <b>25.79</b>       | <b>11.51</b>      | <b>5.76</b>       | <b>3.83</b>       |

## REFERENCES

- [1] C. Szegedy, W. Zaremba, I. Sutskever, J. Bruna, D. Erhan, I. Goodfellow, and R. Fergus, “Intriguing properties of neural networks,” in *Int. Conf. Learn. Represent.*, 2014, pp. 1–10. [1](#), [2](#)
- [2] I. J. Goodfellow, J. Shlens, and C. Szegedy, “Explaining and harnessing adversarial examples,” in *Int. Conf. Learn. Represent.*, 2015, pp. 1–11. [1](#), [2](#), [8](#), [9](#)
- [3] S.-M. Moosavi-Dezfooli, A. Fawzi, and P. Frossard, “Deepfool: a simple and accurate method to fool deep neural networks,” in *IEEE Conf. Comput. Vis. Pattern Recog.*, 2016, pp. 2574–2582. [1](#), [2](#), [3](#)
- [4] N. Carlini and D. Wagner, “Towards evaluating the robustness of neural networks,” in *IEEE Symposium on Security and Privacy*, 2017, pp. 39–57. [1](#), [2](#), [3](#)
- [5] X. Wang, F. Yu, Z.-Y. Dou, T. Darrell, and J. E. Gonzalez, “SkipNet: Learning dynamic routing in convolutional networks,” in *Eur. Conf. Comput. Vis.*, 2018, pp. 409–424. [1](#), [3](#), [4](#), [8](#), [9](#)
- [6] T. Verelst and T. Tuytelaars, “Dynamic convolutions: Exploiting spatial sparsity for faster inference,” in *IEEE Conf. Comput. Vis. Pattern Recog.*, 2020, pp. 2320–2329. [1](#), [3](#), [4](#), [5](#), [8](#), [9](#)
- [7] B. Graham, M. Engelcke, and L. Van Der Maaten, “3D semantic segmentation with submanifold sparse convolutional networks,” in *IEEE Conf. Comput. Vis. Pattern Recog.*, 2018, pp. 9224–9232. [1](#), [3](#), [4](#), [6](#), [10](#)
- [8] A. Krizhevsky *et al.*, “Learning multiple layers of features from tiny images,” *Tech. rep.*, 2009. [2](#), [8](#)
- [9] O. Russakovsky, J. Deng, H. Su, J. Krause, S. Satheesh, S. Ma, Z. Huang, A. Karpathy, A. Khosla, M. Bernstein *et al.*, “Imagenet large scale visual recognition challenge,” *Int. J. Comput. Vis.*, vol. 115, no. 3, pp. 211–252, 2015. [2](#), [8](#)
- [10] A. Dai, A. X. Chang, M. Savva, M. Halber, T. Funkhouser, and M. Nießner, “ScanNet: Richly-annotated 3D reconstructions of indoor scenes,” in *IEEE Conf. Comput. Vis. Pattern Recog.*, 2017, pp. 5828–5839. [2](#), [10](#)
- [11] I. Armeni, O. Sener, A. R. Zamir, H. Jiang, I. Brilakis, M. Fischer, and S. Savarese, “3D semantic parsing of large-scale indoor spaces,” in *IEEE Conf. Comput. Vis. Pattern Recog.*, 2016, pp. 1534–1543. [2](#), [10](#)
- [12] I. Armeni, S. Sax, A. R. Zamir, and S. Savarese, “Joint 2D-3D-semantic data for indoor scene understanding,” *arXiv preprint arXiv:1702.01105*, 2017. [2](#), [10](#)
- [13] J. Behley, M. Garbade, A. Milioto, J. Quenzel, S. Behnke, C. Stachniss, and J. Gall, “SemanticKITTI: A dataset for semantic scene understanding of lidar sequences,” in *Int. Conf. Comput. Vis.*, 2019, pp. 9297–9307. [2](#), [10](#)
- [14] A. Kurakin, I. Goodfellow, S. Bengio *et al.*, “Adversarial examples in the physical world,” pp. 1–10, 2017. [2](#), [3](#), [8](#), [9](#), [10](#)
- [15] A. Madry, A. Makelov, L. Schmidt, D. Tsipras, and A. Vladu, “Towards deep learning models resistant to adversarial attacks,” in *Int. Conf. Learn. Represent.*, 2018, pp. 1–10. [2](#)
- [16] N. Papernot, P. McDaniel, S. Jha, M. Fredrikson, Z. B. Celik, and A. Swami, “The limitations of deep learning in adversarial settings,” in *IEEE European Symposium on Security and Privacy*, 2016, pp. 372–387. [2](#)
- [17] P.-Y. Chen, H. Zhang, Y. Sharma, J. Yi, and C.-J. Hsieh, “ZOO: Zeroth order optimization based black-box attacks to deep neural networks without training substitute models,” in *ACM Workshop on Artificial Intelligence and Security*, 2017, pp. 15–26. [2](#)
- [18] J. Su, D. V. Vargas, and K. Sakurai, “One pixel attack for fooling deep neural networks,” *IEEE Transactions on Evolutionary Computation*, vol. 23, no. 5, pp. 828–841, 2019. [2](#)
- [19] N. Papernot, P. McDaniel, and I. Goodfellow, “Transferability in machine learning: from phenomena to black-box attacks using adversarial samples,” *arXiv preprint arXiv:1605.07277*, 2016. [2](#)
- [20] Y. Dong, F. Liao, T. Pang, H. Su, J. Zhu, X. Hu, and J. Li, “Boosting

adversarial attacks with momentum,” in *IEEE Conf. Comput. Vis. Pattern Recog.*, 2018, pp. 9185–9193. [2](#)

[21] C. Xiang, C. R. Qi, and B. Li, “Generating 3D adversarial point clouds,” in *IEEE Conf. Comput. Vis. Pattern Recog.*, 2019, pp. 9136–9144. [2](#)

[22] D. Liu, R. Yu, and H. Su, “Extending adversarial attacks and defenses to deep 3D point cloud classifiers,” in *IEEE Int. Conf. Image Process.*, 2019, pp. 2279–2283. [2, 10](#)

[23] T. Zheng, C. Chen, J. Yuan, B. Li, and K. Ren, “Pointcloud saliency maps,” in *Int. Conf. Comput. Vis.*, 2019, pp. 1598–1606. [2](#)

[24] D. Liu, R. Yu, and H. Su, “Adversarial shape perturbations on 3D point clouds,” in *Eur. Conf. Comput. Vis.*, 2020, pp. 88–104. [2](#)

[25] Y. Wen, J. Lin, K. Chen, C. P. Chen, and K. Jia, “Geometry-aware generation of adversarial point clouds,” *IEEE Trans. Pattern Anal. Mach. Intell.*, 2020. [2](#)

[26] Z. Xiang, D. J. Miller, S. Chen, X. Li, and G. Kesidis, “A backdoor attack against 3D point cloud classifiers,” in *Int. Conf. Comput. Vis.*, 2021, pp. 7597–7607. [2](#)

[27] M. Haque, A. Chauhan, C. Liu, and W. Yang, “ILFO: Adversarial attack on adaptive neural networks,” in *IEEE Conf. Comput. Vis. Pattern Recog.*, 2020, pp. 14 264–14 273. [2](#)

[28] S. Hong, Y. Kaya, I.-V. Modoranu, and T. Dumitras, “A panda? no, it’s a sloth: Slowdown attacks on adaptive multi-exit neural network inference,” in *Int. Conf. Learn. Represent.*, 2021, pp. 1–17. [2](#)

[29] S. Chen, Z. Song, M. Haque, C. Liu, and W. Yang, “NICGSlowDown: Evaluating the efficiency robustness of neural image caption generation models,” in *IEEE Conf. Comput. Vis. Pattern Recog.*, 2022, pp. 15 365–15 374. [2](#)

[30] A. Krizhevsky, I. Sutskever, and G. E. Hinton, “Imagenet classification with deep convolutional neural networks,” *Adv. Neural Inform. Process. Syst.*, vol. 25, 2012. [2, 3](#)

[31] K. Simonyan and A. Zisserman, “Very deep convolutional networks for large-scale image recognition,” in *Int. Conf. Learn. Represent.*, pp. 1–14. [2, 3](#)

[32] C. Szegedy, W. Liu, Y. Jia, P. Sermanet, S. Reed, D. Anguelov, D. Erhan, V. Vanhoucke, and A. Rabinovich, “Going deeper with convolutions,” in *IEEE Conf. Comput. Vis. Pattern Recog.*, 2015, pp. 1–9. [2](#)

[33] K. He, X. Zhang, S. Ren, and J. Sun, “Deep residual learning for image recognition,” in *IEEE Conf. Comput. Vis. Pattern Recog.*, 2016, pp. 770–778. [2, 3, 8](#)

[34] A. Vaswani, N. Shazeer, N. Parmar, J. Uszkoreit, L. Jones, A. N. Gomez, Ł. Kaiser, and I. Polosukhin, “Attention is all you need,” *Adv. Neural Inform. Process. Syst.*, vol. 30, 2017. [2](#)

[35] Y. Han, G. Huang, S. Song, L. Yang, H. Wang, and Y. Wang, “Dynamic neural networks: A survey,” *IEEE Trans. Pattern Anal. Mach. Intell.*, 2021. [3](#)

[36] T. Bolukbasi, J. Wang, O. Dekel, and V. Saligrama, “Adaptive neural networks for efficient inference,” 2017, pp. 527–536. [3](#)

[37] A. Veit and S. Belongie, “Convolutional networks with adaptive inference graphs,” in *Eur. Conf. Comput. Vis.*, 2018, pp. 3–18. [3, 4](#)

[38] Y. Bengio, N. Léonard, and A. Courville, “Estimating or propagating gradients through stochastic neurons for conditional computation,” *arXiv preprint arXiv:1308.3432*, 2013. [3, 4](#)

[39] C. Herrmann, R. S. Bowen, and R. Zabih, “Channel selection using gumbel softmax,” in *Eur. Conf. Comput. Vis.*, 2020, pp. 241–257. [3](#)

[40] W. Fedus, B. Zoph, and N. Shazeer, “Switch transformers: Scaling to trillion parameter models with simple and efficient sparsity,” *Journal of Machine Learning Research*, vol. 23, no. 120, pp. 1–39, 2022. [3, 4](#)

[41] Z. Xie, Z. Zhang, X. Zhu, G. Huang, and S. Lin, “Spatially adaptive inference with stochastic feature sampling and interpolation,” in *Eur. Conf. Comput. Vis.*, 2020, pp. 531–548. [3, 5](#)

[42] A. Kirillov, Y. Wu, K. He, and R. Girshick, “PointRend: Image segmentation as rendering,” in *IEEE Conf. Comput. Vis. Pattern Recog.*, 2020, pp. 9799–9808. [3](#)

[43] J.-B. Cordonnier, A. Mahendran, A. Dosovitskiy, D. Weissenborn, J. Uszkoreit, and T. Unterthiner, “Differentiable patch selection for image recognition,” in *IEEE Conf. Comput. Vis. Pattern Recog.*, 2021, pp. 2351–2360. [3](#)

[44] L. Yang, Y. Han, X. Chen, S. Song, J. Dai, and G. Huang, “Resolution adaptive networks for efficient inference,” in *IEEE Conf. Comput. Vis. Pattern Recog.*, 2020, pp. 2369–2378. [3](#)

[45] C. Choy, J. Gwak, and S. Savarese, “4D spatio-temporal convnets: Minkowski convolutional neural networks,” in *IEEE Conf. Comput. Vis. Pattern Recog.*, 2019, pp. 3075–3084. [3, 10](#)

[46] X. Zhu, H. Zhou, T. Wang, F. Hong, Y. Ma, W. Li, H. Li, and D. Lin, “Cylindrical and asymmetrical 3D convolution networks for lidar segmentation,” in *IEEE Conf. Comput. Vis. Pattern Recog.*, 2021, pp. 9939–9948. [3, 10](#)

[47] R. Cheng, R. Razani, E. Taghavi, E. Li, and B. Liu, “2-S3Net: Attentive feature fusion with adaptive feature selection for sparse semantic segmentation network,” in *IEEE Conf. Comput. Vis. Pattern Recog.*, 2021, pp. 12 547–12 556. [3](#)

[48] L. Jiang, H. Zhao, S. Shi, S. Liu, C.-W. Fu, and J. Jia, “PointGroup: Dual-set point grouping for 3D instance segmentation,” in *IEEE Conf. Comput. Vis. Pattern Recog.*, 2020, pp. 4867–4876. [3](#)

[49] W. Hu, H. Zhao, L. Jiang, J. Jia, and T.-T. Wong, “Bidirectional projection network for cross dimension scene understanding,” in *IEEE Conf. Comput. Vis. Pattern Recog.*, 2021, pp. 14 373–14 382. [3](#)

[50] Y. Yan, Y. Mao, and B. Li, “Second: Sparsely embedded convolutional detection,” *Sensors*, vol. 18, no. 10, p. 3337, 2018. [3](#)

[51] S. Shi, Z. Wang, J. Shi, X. Wang, and H. Li, “From points to parts: 3D object detection from point cloud with part-aware and part-aggregation network,” *IEEE Trans. Pattern Anal. Mach. Intell.*, 2020. [3](#)

[52] S. Shi, L. Jiang, J. Deng, Z. Wang, C. Guo, J. Shi, X. Wang, and H. Li, “Pv-rcnn++: Point-voxel feature set abstraction with local vector representation for 3D object detection,” *arXiv preprint arXiv:2102.00463*, 2021. [3](#)

[53] A. Athalye, N. Carlini, and D. Wagner, “Obfuscated gradients give a false sense of security: Circumventing defenses to adversarial examples,” 2018, pp. 274–283. [3, 4, 7](#)

[54] X. Glorot, A. Bordes, and Y. Bengio, “Deep sparse rectifier neural networks,” in *Proceedings of the fourteenth international conference on artificial intelligence and statistics*, 2011, pp. 315–323. [3](#)

[55] X. Gao, Y. Zhao, Ł. Dudziak, R. Mullins, and C.-z. Xu, “Dynamic channel pruning: Feature boosting and suppression,” in *Int. Conf. Learn. Represent.*, 2018. [4](#)

[56] R. T. Mullapudi, W. R. Mark, N. Shazeer, and K. Fatahalian, “HydraNets: Specialized dynamic architectures for efficient inference,” in *IEEE Conf. Comput. Vis. Pattern Recog.*, 2018, pp. 8080–8089. [4](#)

[57] C. R. Qi, H. Su, K. Mo, and L. J. Guibas, “PointNet: Deep learning on point sets for 3D classification and segmentation,” in *IEEE Conf. Comput. Vis. Pattern Recog.*, 2017, pp. 652–660. [6](#)

[58] C. R. Qi, L. Yi, H. Su, and L. J. Guibas, “PointNet++: Deep hierarchical feature learning on point sets in a metric space,” 2017, pp. 5105–5114. [6](#)

[59] Y. Wang, Y. Sun, Z. Liu, S. E. Sarma, M. M. Bronstein, and J. M. Solomon, “Dynamic graph CNN for learning on point clouds,” *ACM Trans. Graph.*, vol. 38, no. 5, pp. 1–12, 2019. [6](#)

[60] Y. Liu, B. Fan, S. Xiang, and C. Pan, “Relation-shape convolutional neural network for point cloud analysis,” in *IEEE Conf. Comput. Vis. Pattern Recog.*, 2019, pp. 8895–8904. [6](#)

[61] W. Wu, Z. Qi, and L. Fuxin, “PointConv: Deep convolutional networks on 3D point clouds,” in *IEEE Conf. Comput. Vis. Pattern Recog.*, 2019, pp. 9621–9630. [6](#)

[62] H. Thomas, C. R. Qi, J.-E. Deschaud, B. Marcotegui, F. Goulette, and L. J. Guibas, “KPConv: Flexible and deformable convolution for point clouds,” in *Int. Conf. Comput. Vis.*, 2019, pp. 6411–6420. [6](#)

[63] C. Deng, O. Litany, Y. Duan, A. Poulenard, A. Tagliasacchi, and L. J. Guibas, “Vector neurons: A general framework for  $SO(3)$ -equivariant networks,” in *Int. Conf. Comput. Vis.*, 2021, pp. 12 200–12 209. [6](#)

[64] J. Tu, M. Ren, S. Manivasagam, M. Liang, B. Yang, R. Du, F. Cheng, and R. Urtasun, “Physically realizable adversarial examples for lidar object detection,” in *IEEE Conf. Comput. Vis. Pattern Recog.*, 2020, pp. 13 716–13 725. [7, 8, 11, 12](#)

[65] R. Qian, D. Garg, Y. Wang, Y. You, S. Belongie, B. Hariharan, M. Campbell, K. Q. Weinberger, and W.-L. Chao, “End-to-end pseudo-lidar for image-based 3D object detection,” in *IEEE Conf. Comput. Vis. Pattern Recog.*, 2020, pp. 5881–5890. [7, 8, 11, 12](#)

[66] A. Almahairi, N. Ballas, T. Cooijmans, Y. Zheng, H. Larochelle, and A. Courville, “Dynamic capacity networks,” 2016, pp. 2549–2558. [9](#)